The Astrophysical Journal, 621:663–672, 2005 March 10

INFALL OF THE ELLIPTICAL GALAXY NGC 1404 INTO THE FORNAX CLUSTER

M. Machacek, A. Dosaj, W. Forman, C. Jones, M. Markevitch, A. Vikhlinin, A. Warmflash, and R. Kraft
Harvard-Smithsonian Center for Astrophysics, 60 Garden Street, Cambridge, MA 02138; mmachacek@cfa.harvard.edu
Received 2004 August 6; accepted 2004 November 17

ABSTRACT

We use three *Chandra* observations, totaling 134.3 ks, to constrain the dynamical motion of NGC 1404 falling toward the dominant elliptical NGC 1399 through the Fornax Cluster gas. The surface brightness profile of NGC 1404 shows a sharp edge at ~8 kpc from its center in the direction of NGC 1399, characteristic of jumplike temperature and density discontinuities from ram pressure stripping of the galaxy gas, caused by its motion through the surrounding intracluster medium (ICM). We find that the temperature of the galaxy gas inside the edge is ~2.8 times cooler ($kT = 0.55^{+0.01}_{-0.02}$ keV with abundance $A = 0.73^{+0.65}_{-0.16}\ Z_{\odot}$) than the cluster gas ($kT = 1.53^{+0.10}_{-0.13}$ keV, $A = 0.42^{+0.2}_{-0.13}\ Z_{\odot}$). We use the shape of the surface brightness profile across the edge to fit the position of the edge, the power-law behavior of NGC 1404's density distribution in the leading direction, and the density discontinuity at the edge. The electron density inside the edge $(3.9\text{–}4.3) \times 10^{-3}$ cm^{-3} depends strongly on the gas abundance, while the density of the ICM $(7\text{–}8) \times 10^{-4}$ cm^{-3} depends strongly on the assumed geometry (relative distance) between NGC 1404 and NGC 1399. The corresponding pressure jump of 1.7–2.1 across the leading edge of the galaxy and the cluster free-stream region implies near sonic motion (Mach number 0.83–1.03) for NGC 1404 with a velocity 531–657 km s^{-1} relative to the surrounding cluster gas. The inclination angle of the motion, inferred using the relative radial velocity between NGC 1404 and 1399 as representative of that between NGC 1404 and the cluster ICM, is uncomfortably large ($\gtrsim 40^{\circ}$) given the sharpness of the surface brightness edge, suggesting either a nonzero impact parameter between NGC 1404 and 1399 or that NGC 1399 is also moving radially with respect to the cluster ICM.

Subject headings: galaxies: clusters: general — galaxies: individual (NGC 1404) — intergalactic medium — X-rays: galaxies

Online material: color figures

1. INTRODUCTION

Our early picture of galaxy clusters as simple, dynamically relaxed systems has been changed dramatically over the past decade by X-ray images taken with the *Einstein*, *ROSAT*, Broad Band X-Ray Telescope (BBXRT), and *ASCA* observatories. These images show that galaxy clusters are complex systems with extensive substructure and mergers on timescales of $\sim 10^9$ yr (see, e.g., Forman et al. 2001, 2002 and references therein). The excellent angular resolution of *Chandra* made possible the detailed study of these substructures, particularly near the centers of clusters, revealing surprising new signatures for their interactions. Notably, ram pressure stripping of subcluster gas due to its motion through the intracluster medium (ICM) was found to produce prominent X-ray surface brightness discontinuities from cold fronts (dense surviving subcluster cores) rather than from the shocked gas also expected from such motion (Forman et al. 2001, 2002; Vikhlinin et al. 2001; Markevitch et al. 2000; Heinz et al. 2003). Furthermore, high-quality X-ray measurements of the geometry and gas properties along the interface between the cold front and the ICM were used to determine the dynamical motion of the cold front through the cluster (Vikhlinin et al. 2001; Mazzotta et al. 2001).

Galaxies in these dynamically rich cluster environments are subject to both tidal and hydrodynamic interactions that significantly affect their evolution (see, e.g., Gnedin 2003; Acreman et al. 2003 and references therein). *Chandra* has also made possible detailed studies of hot gas in member galaxies of nearby clusters in interaction with each other and their gaseous environment. Just as in the case of larger cluster substructure, the action of ram pressure acting on gas within an individual galaxy, which is due to the galaxy's motion through the ICM, produces sharp X-ray surface brightness discontinuities along the galaxy's leading edge associated with cold fronts, as well as trailing wakes and comet-like debris tails of gas swept from the infalling system (e.g., see Forman et al. 1979; White et al. 1991; Rangarajan et al. 1995 for M86; Irwin & Sarazin 1996 for NGC 4472, both in Virgo; and Wang et al. 2004 for C153 in A2125). Thus, in addition to elucidating the hydrodynamics of ram pressure stripping itself, high-quality X-ray measurements of the geometry of these features, combined with measurements of the gas temperatures, abundances, and densities along the interface between the cold front and the ICM, may be used to constrain the three-dimensional (transverse as well as radial) motion of the galaxy through the cluster (Dosaj et al. 2002).

In this paper we present this analysis for one such galaxy, NGC 1404 (shown in Fig. 1), which is undergoing ram pressure stripping as it falls inward toward the Fornax Cluster center in the direction of the dominant elliptical galaxy NGC 1399. Both NGC 1399 and 1404 are well studied in X-rays. Early observations of NGC 1399 using *EXOSAT*, *Einstein* IPC, *Ginga*, and BBXRT (see Jones et al. 1997 and references therein) established the presence and mean temperature of its X-ray–emitting halo. More recent measurements by *ASCA*, *ROSAT*, *XMM-Newton*, and *Chandra* mapped the temperature and density profiles for the galaxy and the surrounding Fornax ICM (Jones et al. 1997; Buote 2002; Paolillo et al. 2002; O'Sullivan et al. 2003; Scharf et al. 2004). NGC 1404 has been observed with *ASCA* (Loewenstein et al. 1994; Buote & Fabian 1998), *ROSAT* PSPC (Jones et al. 1997; Paolillo et al. 2002; O'Sullivan et al. 2003), and *Chandra* (Forman et al. 2002; Dosaj et al. 2002;

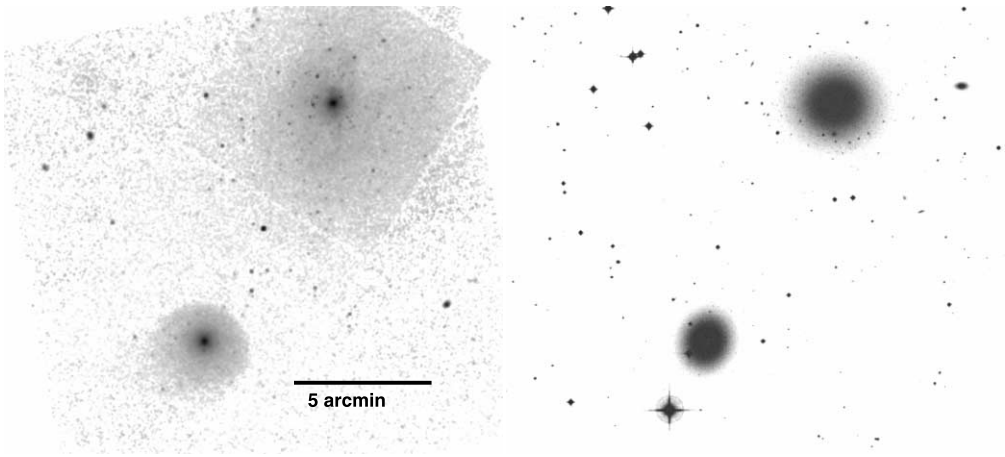

FIG. 1.—0.3–2.0 keV ACIS X-ray (*left*) and DSS (*right*) images of NGC 1404 (southeast, *lower left*) and NGC 1399 (northwest, *upper right*) galaxies in the Fornax Cluster. The X-ray images from three *Chandra* observations have been binned by 2 into 0.″984 image pixels, background subtracted, exposure corrected, and co-added in WCS coordinates before smoothing with a 2″ Gaussian. The image color scale has a logarithmic stretch from 10^{-9} to 6×10^{-6} photons s^{-1} cm^{-2} arcsec^{-2}. The bright elliptical galaxy NGC 1404 exhibits a surface brightness discontinuity along its northwestern edge at a radius of ∼1.′4 (8 kpc) from its center. [*See the electronic edition of the Journal for a color version of this figure.*]

Scharf et al. 2004; this work). The temperature of diffuse gas in NGC 1404 was found to be approximately isothermal, with $kT \sim 0.6$ keV. The higher temperature ($kT \sim 0.75$ keV) found by Loewenstein et al. (1994) was most likely a result of the large radius (3′) aperture used (which was due to the *ASCA* point-spread function), which extended well beyond the effective radius of NGC 1404. With the much better *ROSAT* PSPC resolution, Jones et al. (1997) found an asymmetric surface brightness distribution, strongly suggesting that NGC 1404 was undergoing ram pressure stripping. Also using *ROSAT* PSPC data, Paolillo et al. (2002) measured the surface brightness asymmetry between the leading (northwest) sector and trailing (southeast) sector of NGC 1404, showing the steep gradient in the surface brightness in the northwest sector at $r \sim 90''$ (8 kpc), while O'Sullivan et al. (2003) observed a temperature jump for $r > 2'$, across the leading edge of the galaxy and the surrounding Fornax ICM.

In Figure 1 we present the 0.3–2 keV co-added image from three *Chandra* observations, totaling 134.3 ks (detailed in § 2), of NGC 1404 falling toward the dominant cluster elliptical galaxy NGC 1399 (*left panel*). For comparison we also show the Digitized Sky Survey optical image matched in WCS coordinates (*right panel*). NGC 1399 is located in the northwest (*upper right*) corner of each panel, while the bright elliptical galaxy NGC 1404 is located ∼54 kpc (9.′8) in the plane of the sky to the southeast (*lower left corner*). The X-ray images have been individually background subtracted and corrected for telescope vignetting and spatial efficiency variations by means of exposure maps generated with standard CIAO tools, assuming a fixed spectral energy of 0.9 keV. We clearly see the sharp edge in the surface brightness on the northwest side of NGC 1404 (in the direction of NGC 1399), formed by gas bound to NGC 1404 shaped by the ram pressure of the cluster gas, and also the characteristic tail of ram pressure–stripped gas to the galaxy's southeast. We use data from these three *Chandra* observations to measure the temperature and density of gas on either side of the surface brightness edge and calculate the dynamical motion of NGC 1404 relative to the Fornax ICM. This is an extension of earlier work on the Fornax Cluster by Dosaj et al. (2002) using the *Chandra* ACIS-S observation (ObsID 319) to estimate the motion of NGC 1404 toward 1399, and it complements the recent, similar work by Scharf et al. (2004) using ACIS-I observations. Both assumed that the motion was primarily in the plane of the sky and, from the jump in gas pressure, obtained infall velocities of 466 ± 38 km s^{-1} (Dosaj et al. 2002) and 660 ± 260 km s^{-1} (Scharf et al. 2004).

Our discussion is organized as follows: In § 2 we describe the observations and our data reduction and processing procedures. In § 3 we discuss our analysis method and main results. In § 3.1 we use spectral analyses to determine the temperature inside the surface brightness edge for NGC 1404 and outside the edge in the surrounding Fornax ICM, showing that gas within the surface brightness edge is a factor of ∼3 cooler than the surrounding cluster gas. In § 3.2 we use co-added *Chandra* images from the three observations of NGC 1404 to extract the X-ray surface brightness profile across the edge and model the geometry of the cold front. We combine these data with the spectral information to construct the corresponding electron density profile across the edge, and in § 3.3 we calculate the velocity of NGC 1404 relative to the Fornax ICM. In § 4 we briefly summarize our results. Unless otherwise indicated, all errors are 90% confidence levels and coordinates are J2000.0. Assuming a Hubble constant $H_0 = 75$ km s^{-1} Mpc^{-1} in the currently preferred flat ΛCDM cosmology ($\Omega_m = 0.3$, $\Omega_\Lambda = 0.7$) and a redshift $z = 0.004753$, the redshift of the dominant elliptical galaxy NGC 1399, as representative for the Fornax Cluster, the luminosity distance to the cluster is 19 Mpc (Paolillo et al. 2002) and 1′ corresponds to a distance scale of 5.49 kpc.

2. OBSERVATIONS AND DATA REDUCTION

Our data consist of three observations of galaxies NGC 1404 and 1399 in Fornax taken with *Chandra* using the Advanced CCD Imaging Spectrometer array (ACIS; Garmire et al. 1992; Bautz et al. 1998): a 57.4 ks exposure taken on 2000 January 18–19 (when the focal plane temperature of the instrument was −110°C) using chips S2 and S3 (ObsID 319), a 29.6 ks exposure (of NGC 1404 alone) taken on 2003 February 13 using the S3 chip (ObsID 2942), and a 47.3 ks exposure taken on 2003 May 28–29 using the ACIS-I array (ObsID 4174). For ObsID 2942 and 4174 the focal plane temperature was −120°C throughout the observation. Each CCD chip is a 1024×1024 pixel array where each pixel subtends $0.''492 \times 0.''492$ on the sky.

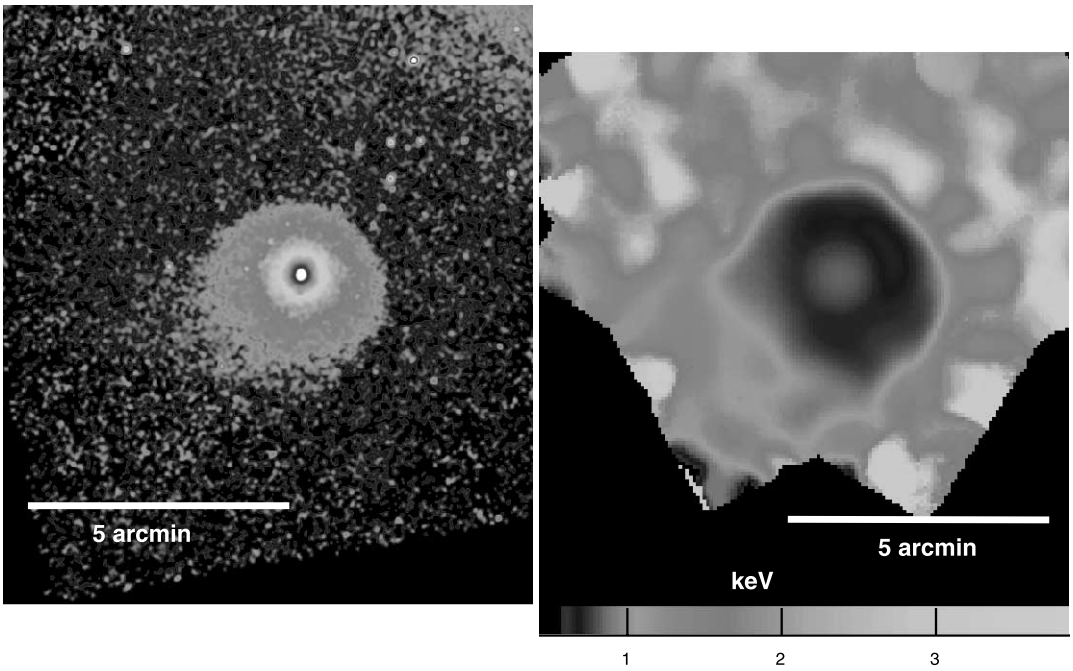

FIG. 2.—Surface brightness (*left*) and temperature map (*right*), matched in WCS coordinates, for NGC 1404 and the surrounding region. [*See the electronic edition of the Journal for a color version of this figure*.]

The data were analyzed using the standard X-ray processing packages CIAO version 3.0.2, FTOOLS, and XSPEC version 11.2. We corrected for the increased charge transfer inefficiency on the frontside-illuminated chips caused by exposure to low-energy protons during passages of the telescope through the Earth's radiation belts shortly after launch (Prigozhin et al. 2000), as well as for the time-dependent declining efficiency of the ACIS detector due to the buildup of contaminants on the optical filter (Plucinsky et al. 2003), which is important at energies below 1.5 keV. Filtering removed events with bad grades (1, 5, and 7) and any events falling on hot pixels. Periods of anomalously high background (flares) were identified and were removed from the data along with periods of anomalously low count rates at the beginning and end of each observation. This resulted in useful exposure times of 56,241, 29,299, and 41,478 s, respectively, for the observations.

Backgrounds for these observations were created from the source-free (blank sky) background sets appropriate for the CCDs, dates of observation, and instrument configurations of interest.[1] These were the merged 201,452 s (114,886 s) period B source-free data set for the S2(S3) chip with ACIS-S at the aimpoint for ObsID 319, the merged 450,000 s period D source-free data set for the S3 chip with ACIS-S at aimpoint for ObsID 2942, and the merged 550,000 s period D source-free data set for the ACIS-I array with ACIS-I at the aimpoint for ObsID 4174. Identical cleaning, energy, and spatial filters were applied to source and background data throughout, so that the normalization of the background is set, in each case, by the ratio of exposure times. We checked this normalization by comparing count rates between the source and background files in the 9–12 keV range where particle background dominates. The source count rates were found to differ by $\lesssim$3.5% from those of the blank-sky sets for ObsID 319 and 2942, but were anomalously high ($\sim$16%) for ObsID 4174. We normalized the blank-sky sets for that observation to agree with the observed 9–12 keV source count rates. Thus, we adopt 3.5% as the remaining uncertainty in the background levels for the three data sets. We identified point sources in the $16.'8 \times 16.'8$ field of the combined data in the 0.3–10 keV energy band using a multiscale wavelet decomposition algorithm set with the detection threshold at 5 σ. The resulting 220 source identifications were excluded from the following spectral and surface brightness analyses. We refer the reader to Angelini et al. (2001) for a detailed analysis of the point-source population of this system.

[1] See http://cxc.harvard.edu/contrib/maxim/acisbg.

3. RESULTS

In Figure 2 we present surface brightness and temperature maps of the galaxy that clearly show the general structure of the X-ray emission from NGC 1404 and the surrounding ICM, i.e., a sharp, bow-shaped drop in surface brightness that is correlated to a similarly shaped jump in temperature. In the northwest direction (the leading edge) the bow-shaped edge is nearly circular, while at larger angles the emission merges into a comet-like tail. In order to isolate the leading edge, we trace the surface brightness discontinuity with an elliptical segment centered at WCS coordinates ($3^h38^m52^s.1$, $-35^\circ35'39''.6$) with major (minor) axes of 8.3 (8.0) kpc and position angle $19^\circ.94$. The center of this edge-bounding ellipse is offset by $\lesssim 2''.4$ to the east of the optical center of NGC 1404. We construct the surface brightness profile for the exposure-corrected, co-added image using elliptical annuli concentric to the edge-bounding ellipse and constrained to lie within an angular sector extending from 35° to $91^\circ.4$ measured counterclockwise from east (see Fig. 3). For the surface brightness profile, radial intervals are chosen to increase (decrease) with logarithmic step size 1.05 as the radial distance is increased (decreased) from the position of the bounding ellipse. We need to obtain corresponding temperatures for gas in these regions. However, in order to obtain sufficient statistics for spectral analysis, we increase the logarithmic step size outside

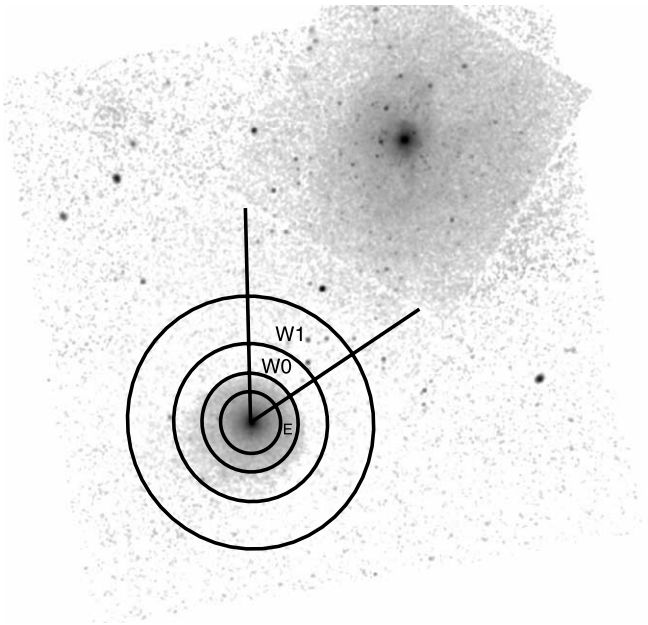

FIG. 3.—Regions used in the edge analysis. The surface brightness profiles are extracted in elliptical annuli concentric to those shown and lying within the angular sector shown (from 35° to 91°.4 measured counterclockwise from the east). Spectral extraction regions W0 and W1 for the cluster gas outside the edge are also constrained to lie within that angular sector, while the full elliptical annulus E is used for the spectrum of NGC 1404 just inside the edge. [*See the electronic edition of the Journal for a color version of this figure.*]

the bounding ellipse to 1.16. These spectral extraction regions are shown in Figure 3. We interpret region W1 as being representative of the undisturbed, free-streaming Fornax Cluster gas and region W0 as cluster gas directly outside the edge (Vikhlinin et al. 2001). To determine the spectral properties of gas inside the edge, we use the elliptical annulus denoted by E in Figure 3 to maximize statistics, in order to sharpen our determination of the metal abundance in NGC 1404, as well as the gas temperature inside the edge.

3.1. *Gas Temperatures*

Spectra from both ObsID 2942 and 4174 were fitted simultaneously with XSPEC version 11.2 over the 0.3–5 keV energy range using APEC emission models for collisionally ionized diffuse gas (Smith et al. 2001), corrected for absorption using Wisconsin photoelectric cross sections (Morrison & McCammon 1983). ObsID 319 was not used in the spectral analysis because of calibration uncertainties for period B observations. Counts were grouped with a predefined grouping, resulting in channels of approximately constant logarithmic width. The hydrogen column density was initially fixed at its Galactic value, 1.45×10^{20} cm^{-2} (Dickey & Lockman 1990), with the gas temperature and abundance taken as free parameters. The hydrogen absorbing column was then allowed to vary to check the stability of the fit. The data showed no need for increased absorption either in the cluster gas or in the outer elliptical region E in NGC 1404, just inside the edge.

The results of the spectral analyses are summarized in Table 1. The best fits for the cluster free-stream region (W1) and for the galaxy emission inside the edge (E) are shown in Figure 4. We find a temperature ($1.53^{+0.10}_{-0.13}$ keV) and abundance ($0.42^{+0.2}_{-0.13}$ $Z_\odot$) for gas in the free-stream region. These values are in excellent agreement with *XMM-Newton* measurements for diffuse gas $\sim 8'$ from NGC 1399 ($\sim 2'$ from NGC 1404) by Buote (2002), who finds the data at large radius from NGC 1399 to be well represented by a single-temperature APEC model with temperature $kT = 1.35 \pm 0.15$ keV (errors 1 σ) and abundance $A \sim 0.4$–0.6 $Z_\odot$. They are also in reasonable agreement with Jones et al. (1997), who find $kT = 1.26^{+0.08}_{-0.11}$ keV and $A = 0.51^{+0.23}_{-0.16}$ $Z_\odot$ for radii $r \sim 8'$–$10'$ from NGC 1399; O'Sullivan et al. (2003), who find at the same radius $kT \sim 1.2$–1.45 keV and $A \sim 0.4$–0.7 $Z_\odot$ (see their Fig. 1) using *ROSAT* PSPC data; and Scharf et al. (2004), who find $kT \sim 1.6$ keV using *Chandra* ACIS-I data.

Because of limited statistics, we are unable to freely vary all the parameters of the fit for region W0, the diffuse gas just outside the edge containing the stagnation region. We fix the abundance at the best-fit value for region W1 and allow the temperature to vary. We find a temperature $1.66^{+0.25}_{-0.15}$ keV consistent with that for region W1 given the large errors. The somewhat cooler temperature (~ 1 keV) measured by O'Sullivan et al. (2003) with *ROSAT* data when using a circular annulus with mean radius $2'$ (11 kpc) centered on NGC 1404 is most likely due to the fact that such a circular region contains cooler ram pressure–stripped gas from the trailing side of NGC 1404 (the debris tail) as well as the Fornax ICM.

A single-temperature APEC model provides a poor fit to the data inside the edge, as shown in Table 1. This is not surprising, since a second component is warranted to model the contribution from cluster emission. We model this emission with a separate APEC component with abundance and temperature fixed at the best-fit cluster values. We find a temperature for the galactic diffuse gas inside the edge of $0.55^{+0.01}_{-0.02}$ keV with an abundance $0.73^{+0.65}_{-0.16}$ $Z_\odot$. The fit is unchanged if the cluster

TABLE 1
APEC MODEL SPECTRAL FITS

Region	R_{in} (kpc)	R_{out} (kpc)	Source II (counts)	Source III (counts)	kT (keV)	A ($Z_\odot$)	Λ (10^{-23} ergs cm^3 s^{-1})	χ^2/dof
NGC 1404 E	5.1	8.2	4071	2790	...	...	...	...
One component	...	...	...	...	0.58 ± 0.01	0.32 ± 0.05	1.0	337/187
Two component	...	...	...	...	1.53^f	0.42^f	...	...
	...	...	...	...	$0.55^{+0.01}_{-0.02}$	$0.73^{+0.65}_{-0.16}$	1.9	276/185
Fornax W0	8.2	13	333	328	$1.66^{+0.25}_{-0.15}$	0.42^f	...	11.2/20
Fornax W1	13	21	930	710	$1.53^{+0.10}_{-0.13}$	$0.42^{+0.2}_{-0.13}$	0.846	104.5/69

NOTES.—The second and third columns list the inner and outer radii of each extraction region shown in Fig. 3, measured from the center of the bounding ellipse. Source II (III) are the background-subtracted source counts in the 0.3–5 keV energy band for ObsID 2942 (4174). Superscript f denotes a fixed parameter. Λ denotes the X-ray emissivity (cooling function) derived from XSPEC for the 0.3–2 keV energy band. Errors are 90% confidence limits.

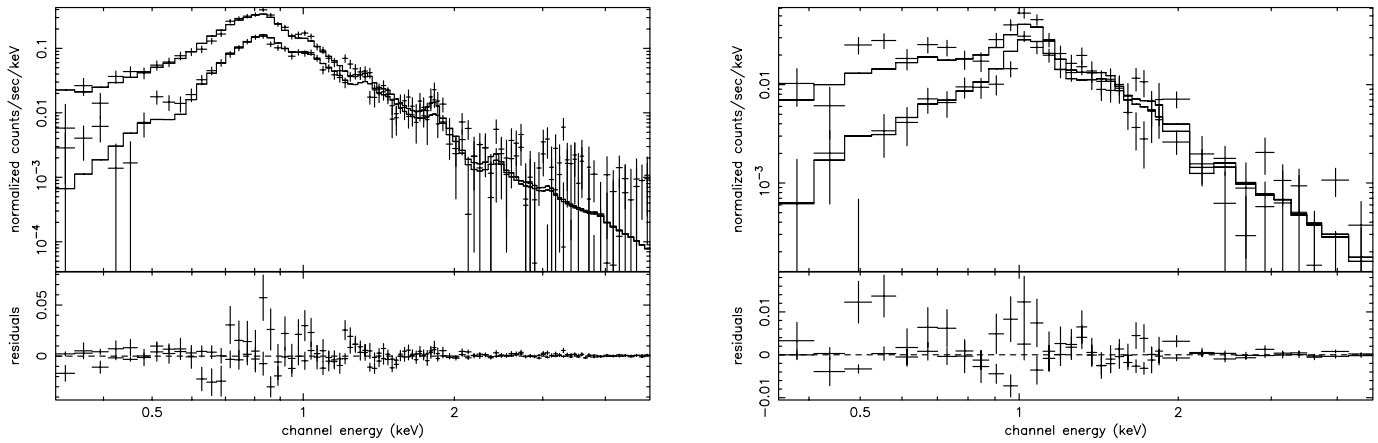

FIG. 4.—*Left*: Best simultaneous two-temperature APEC model fit to ObsID 2942 and 4174 data for the elliptical annulus (E, shown in Fig. 3) just inside the edge, where the second component models the cluster emission. *Right*: Best simultaneous single-temperature APEC model fit to ObsID 2942 and 4174 data for the Fornax Cluster gas in the free-stream region (W1 shown in Fig. 3). Absorption is fixed at the Galactic value ($n_{\rm H} = 1.45 \times 10^{20}$ cm^{-2}) in each region.

component temperature is allowed to vary, although the errors on the fitted cluster temperature ($1.48^{+0.24}_{-0.22}$ keV) are large. We also obtain a reasonable fit ($\chi^2/{\rm dof} = 298/185$) using an APEC+power law model. We find the gas properties of the thermal component ($kT = 0.56 \pm 0.01$ keV, $A = 0.69^{+0.23}_{-0.27}\ Z_\odot$, $\Lambda = 1.8^{+0.5}_{-0.6} \times 10^{-23}$ ergs cm^3 s^{-1}), which are in agreement with those found for the two-component APEC model listed in Table 1, and a photon index ($\Gamma = 2.1^{+0.2}_{-0.4}$) consistent with that expected for a population of unresolved X-ray binaries.

The temperature we measure for diffuse gas in NGC 1404 is in good agreement with previous measurements given the differences in the models and spectral extraction regions. Using *ROSAT* PSPC data, Jones et al. (1997) found a mean temperature for NGC 1404 of $0.65^{+0.02}_{-0.01}$ keV, while O'Sullivan et al. (2003) found a temperature profile consistent with isothermal with $kT = 0.6 \pm 0.01$ for radii $r \lesssim 1\farcm6$, similar to that found by Scharf et al. (2004) using ACIS-I data. We find, however, an abundance A higher than that found by most previous authors ($A \sim 0.14\ Z_\odot$, Loewenstein et al. 1994; $A \sim 0.16\ Z_\odot$, Jones et al. 1997; $A \sim 0.35$, O'Sullivan et al. 2003) and more consistent with the solar or supersolar abundances expected for elliptical galaxies (Buote 2002; Brighenti & Mathews 1999). This discrepancy is probably due to a combination of limited statistics, large heterogeneous extraction regions, the use of simple single-temperature models, and/or incomplete modeling of unresolved X-ray binaries in those previous studies. We are in agreement with the abundance measurement ($A = 0.7^{+2}_{-0.3}$) for NGC 1404 found by Buote & Fabian (1998) using a multitemperature MEKAL model to describe the ASCA data.

In Table 1 we also list the X-ray emissivity (cooling function) Λ derived from the XSPEC best-fit models for the energy range 0.3–2.0 keV, the energy band we used for the surface brightness profiles in § 3.2. In contrast to cluster analyses, where the X-ray emissivity is dominated by the continuum free-free emission and depends only weakly on temperature and abundance (Vikhlinin et al. 2001), the emissivity of cool, metal-rich gas in galaxies is dominated by line emission and in this case varies by more than a factor of 2 between X-ray–emitting gas in the cluster and that in the galaxy. Since the X-ray surface brightness depends on the product of the emission measure and the X-ray emissivity, high-quality abundance measurements in galaxies are crucial for determining accurate electron densities from surface brightness profiles and subsequently constraining the dynamical motion of the system.

3.2. *Fitting the Surface Brightness Edge*

In Figure 5 we plot the X-ray surface brightness profile for NGC 1404, constrained by the wedge geometry shown in Figure 3 to sample only the region across the leading edge of the galaxy, as a function of the mean projected distance from the center of the edge-bounding ellipse. Three distinct regions are apparent. For small radii the data are well described by a power law (PL) with a break at $\sim$4 kpc. For radii 4 kpc $\lesssim r \lesssim$ 8 kpc we see the surface brightness profile characteristic of a sharp edge, where the surface brightness decreases by $\sim$1 order of magnitude over a radial range of $\sim$1–2 kpc. This is characteristic for the motion of a spheroid through a uniform gas and is consistent with a jumplike density discontinuity at the boundary. Outside the edge ($r > 8$ kpc), we see a surface brightness profile consistent with cluster gas, with a possible enhancement at $r \sim 10$ kpc, near the edge. The gradual rise in surface brightness for $r > 20$ kpc ($\lesssim$34 kpc from NGC 1399) is due to halo emission from NGC 1399 (see Fig. 6).

In order to fit the surface brightness in Figure 5, we need to model the form of the electron density in the galaxy NGC 1404 and the Fornax ICM. We assume, as in Vikhlinin et al. (2001), that the cold front inside the edge can be described by an isothermal sphere whose density is well modeled by a PL,

$$n_e(r < r_{\rm edge}) = A_{\rm edge}\left(\frac{r}{r_{\rm edge}}\right)^{-\alpha}, \qquad (1)$$

where $r_{\rm edge}$ is the position of the edge and $A_{\rm edge}$ is the electron density in the cold front inside the galaxy at the position of the edge ($r = r_{\rm edge}$).

The density model for the cluster emission is more problematic, since it requires knowledge of the density profile across the full extent of the cluster along the line of sight ($r \lesssim 1.5$ Mpc) and may contain local variations due to the presence of significant subcluster mass concentrations common in dynamically young clusters (see, e.g., Schindler et al. 1999 for Virgo; Machacek et al. 2002 and AbdelSalam et al. 1998 for A2218; and Drinkwater et al. 2001 for Fornax). We adopt simple isothermal β-models for the surface brightness and gas density of the Fornax Cluster gas outside the edge, such that the surface brightness $S(r)$ is given by

$$S(r) = S_0\left[1 + \left(\frac{r}{r_c}\right)^2\right]^{-3\beta+0.5}, \qquad (2)$$

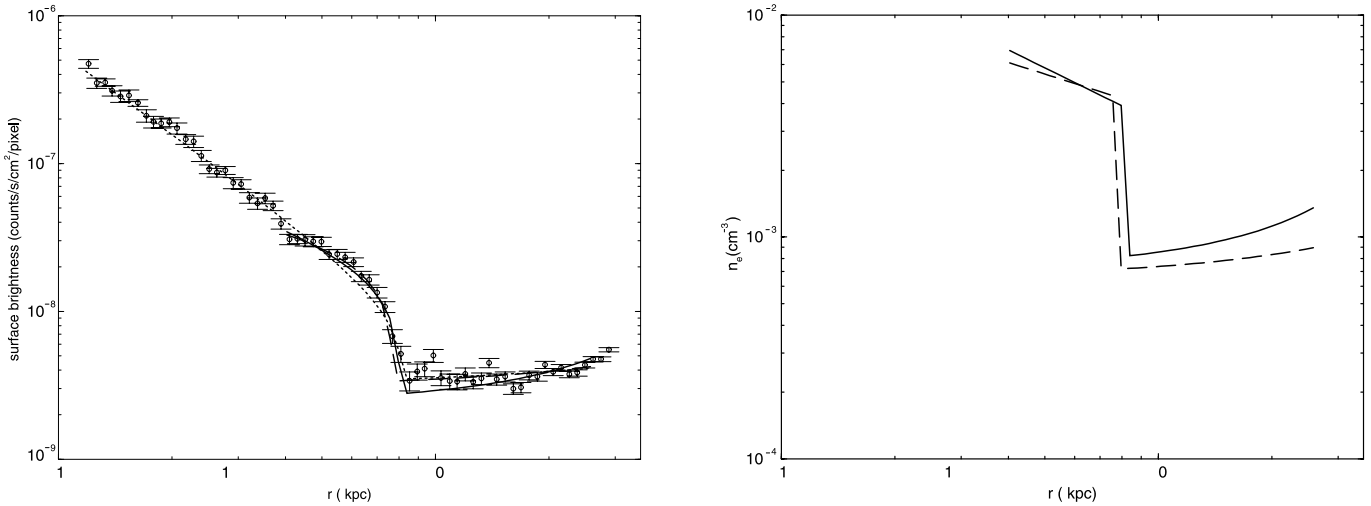

FIG. 5.—*Left*: Surface brightness profile across the edge from elliptical annuli bounded by the sector shown in Fig. 3 as a function of the distance from the center of the bounding ellipse. The models shown represent PL density distributions inside the edge (4 kpc $\lesssim r \lesssim r_{\rm edge}$) and two β-model fits to the Fornax ICM ($r > r_{\rm edge}$): $\beta = 0.35$, $r_c = 45''$ from Jones et al. (1997; PL+ICM1, *solid line*) and $\beta = 0.3$, $r_c = 394''$ (PL+ICM2, *dashed line*) from a three-component β-model fit to NGC 1399. The dotted line shows the best fit for an SPL model for radii 1 kpc $\lesssim r < r_{\rm edge}$ inside the edge and the ICM2 model outside the edge. *Right*: Corresponding electron density profiles for PL+ICM1 (*solid line*) and PL+ICM2 (*dashed line*) models showing the electron density discontinuity across the edge.

where $S(r)$ is the surface brightness at a given radius, S_0 is the central surface brightness, and r_c is the core radius. Then the corresponding electron density is given by

$$n_e(r) = n_0 \left[1 + \left(\frac{r}{r_c}\right)^2\right]^{-3\beta/2}. \quad (3)$$

In Figure 6 we show two multiple-component β-model fits to the surface brightness profile of NGC 1399 with point sources and emission from NGC 1404 excluded, where the fit to the data is the sum of individual components given by equation (2). In each case the innermost central region is modeled with $r_c = 6''$ and $\beta = 0.65$. This result is in good agreement with the fit to NGC 1399 by O'Sullivan et al. (2003), who find $r_c = 6''.6 \pm 0''.6$ and $\beta = 0.59 \pm 0.1$, although they use an elliptical β-model with axis ratio 1.23 rather than our spherically symmetric one.

Surface brightness profiles at larger radii have been measured by Jones et al. (1997) and Paolillo et al. (2002) using *ROSAT* PSPC data. Jones et al. (1997) found the surface brightness profile beyond the core of NGC 1399 to be well represented by a single β-model with core radius $r_c = 45''$ and $\beta = 0.35$ out to a radius of $40'$ (220 kpc). Paolillo et al. (2002) modeled the surface brightness profile of NGC 1399 and the Fornax ICM with a three-component β-model whose third (cluster) component dominated emission beyond $7'$. Their model is consistent with the model of Jones et al. (1997) for radii $r \lesssim 200$ kpc, where the *ROSAT* PSPC corrections are well known, but falls off more rapidly at larger radii.

Similarly, we find our data equally well described by either a two- or three-component model over the radial range of our observation. The left panel of Figure 6 models the data with a two-component β-model, where the outer component is parameterized by $r_c = 45''$ and $\beta = 0.35$, hereafter called ICM1, as

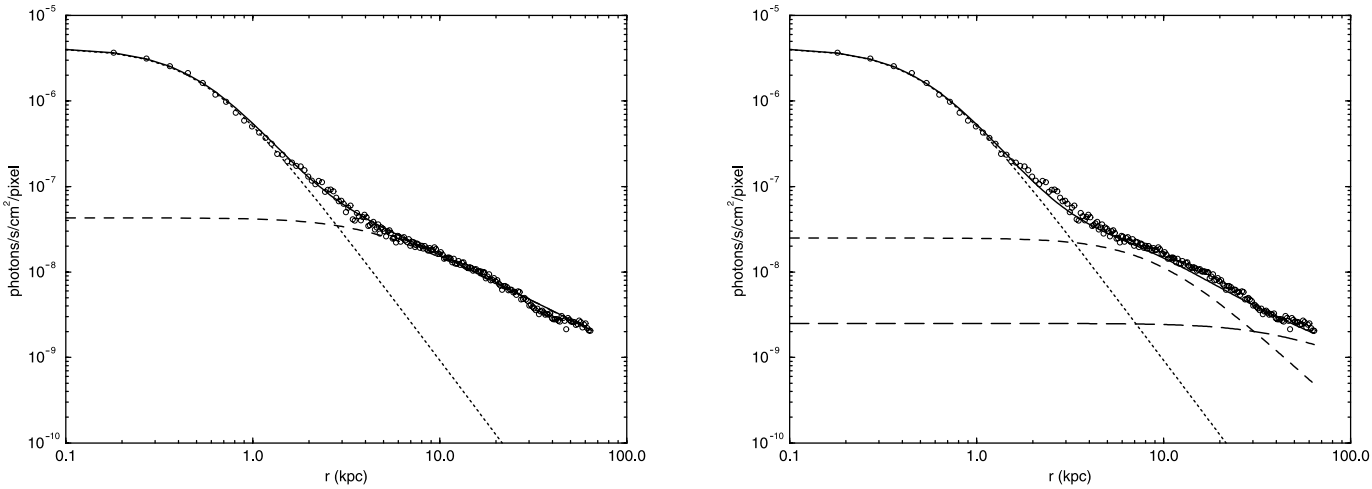

FIG. 6.—β-model fits to the surface brightness profile of NGC 1399 as a function of the radial distance from the center of NGC 1399. *Left*: Two-component fit with (r_c, β) given by ($6''$, 0.65; *dotted line*) and ($45''$, 0.35; *dashed line*) for the core and outer regions, respectively. *Right*: Three-component fit with r_c, β for the core, halo, and cluster given by ($6''$, 0.65; *dotted line*), ($98''$, 0.5, *dashed line*), and ($394''$, 0.3; *long-dashed line*), respectively. The solid line denotes the sum of the components in each case.

found by Jones et al. (1997). The right panel shows a three-component β-model fit to the same data, where the surface brightness at large radii is described by the sum of a central component with (r_c, β) the same as above and two additional components, the galactic halo gas with ($r_c = 98''$, $\beta = 0.5$) and cluster gas with ($r_c = 394''$, $\beta = 0.3$), hereafter called ICM2. The surface brightness edge in NGC 1404 is located at a projected distance of $\sim$46 kpc from the center of NGC 1399, where the second (third) β-model component in the two (three) component fit dominates. Since this represents the minimum physical distance between the edge and the center of the dominant cluster elliptical galaxy NGC 1399 (and the overlap between components in this region is small), we adopt the density β-model from equation (3), with parameters fixed by those components, as representative of the Fornax Cluster gas in our analysis of the edge. Our data do not probe cluster distances large enough to distinguish between these two density models. Thus, we consider both models in order to investigate how uncertainties in the cluster density distribution at large distances affect our results.

In order to extract the density distribution from the surface brightness profiles, we need to make additional assumptions about the relative three-dimensional geometry of NGC 1404 with respect to NGC 1399. The comet-like tail to the southeast of NGC 1404 seen in Figures 1 and 3 is evidence for the ram pressure stripping of gas from NGC 1404. Since ram pressure stripping is more likely in the denser, central regions of the cluster (i.e., near the dominant elliptical galaxy NGC 1399), we assume that NGC 1404 and 1399 both lie near the plane of the sky, such that the projected distance 9.′8 is representative of their physical radial separation. The direction of the tail, pointing to the southeast and away from the direction of motion, indicates that NGC 1404 is moving to the northwest toward NGC 1399. Finally, the sharpness of the edge suggests that we are able to directly view the stagnation region such that the inclination of the motion with respect to the plane of the sky should not be too large (Mazzotta et al. 2001). These are the same assumptions used in the analysis of the infalling subcluster in A3667 (Vikhlinin et al. 2001). Our analysis method closely follows that work.

We calculate the surface brightness by integrating the square of the density times the corresponding X-ray emissivity, given in the eighth column of Table 1, along the line of sight. The data are fitted, using a multivariate χ^2 minimization scheme, allowing the position of the edge ($r_{\rm edge}$), density PL index inside the edge (α), and galaxy electron density at the edge ($A_{\rm edge}$) to vary. We also allow the cluster density normalization (n_0 in eq. [3]) to be a free parameter to partially compensate for possible local density fluctuations in the cluster ICM when extracting the cluster electron density near the edge.

In Figure 5 we show the results for three density models: a PL density model for the edge region (4 kpc $< r < r_{\rm edge}$) interior to NGC 1404 with the cluster density modeled by either ICM1 or ICM2, and a single–power-law (SPL) model for $r > 1$ kpc, with no break at $r \sim 4$ kpc. The ICM2 model is used for the cluster density in this latter case. As the dotted line in Figure 5 shows, the surface brightness profile for radii $\lesssim$4 kpc is well reproduced by this simple PL density model for the galaxy (SPL+ICM2), with a best-fit PL index $\alpha = 1.54$ (corresponding to a β-model with $\beta = 0.47$ for $r \gg r_c$), in reasonable agreement with the β-model results ($\beta = 0.51$, $r_c = 0.57$ kpc) for NGC 1404 by Paolillo et al. (2002) and ($\beta \sim 0.5$) Scharf et al. (2004). However, this model is unable to reproduce the shape of the surface brightness distribution in the edge region (4 kpc $< r < r_{\rm edge}$). Both density models, PL+ICM1 (*solid line*) and PL+ICM2 (*dashed line*), reproduce the surface brightness profile across the edge well. The fit parameters for these models are summarized in Table 2. The electron densities derived from the surface brightness profile depend on the square root of the cooling function, $\Lambda^{1/2}$. For clarity, we also list in Table 2 the electron densities derived from the surface brightness profile of Figure 5, using the cooling functions for the best-fit APEC model (region W1) for the Fornax ICM and the two-component APEC model for NGC 1404 listed in Table 1. These mean densities, derived by fitting the surface brightness profile directly for gas inside the edge (3.9×10^{-3} cm^{-3} for the PL+ICM1 model and 4.3×10^{-3} cm^{-3} for the PL+ICM2 model), are in excellent agreement with the β-model result ($\sim 4 \times 10^{-3}$ cm^{-3}) by Scharf et al. (2004), although our value for the cluster gas is $\sim$20% higher. For the cluster emission, the measured temperatures are $\sim$1.5 keV, so that the uncertainty in the derived cluster density due to the uncertainty in the abundance is $\lesssim$6%. For emission inside the edge of NGC 1404, where the temperature is cooler, the uncertainty in the electron density due to the uncertainty in our measured values of the abundance is larger, $\sim$25%.

TABLE 2
Best-Fit Edge Position and Electron Densities

Property	PL+ICM1 Model	PL+ICM2 Model
$r_{\rm edge}$ (kpc)	8.01	7.64
α	0.84	0.54
$n_{\rm in}$ (10^{-3} cm^{-3})	3.9	4.3
$n_{\rm out}$ (10^{-3} cm^{-3})	0.82	0.72

Notes.—$r_{\rm edge}$ is the position of the edge measured from the center of the bounding ellipse in Fig. 3, α is the PL index of the spherically symmetric electron density distribution inside the edge, and $n_{\rm in}$ ($n_{\rm out}$) is the electron density just inside (outside) the edge.

3.3. *Bounding the Galaxy's Dynamical Motion*

Following Vikhlinin et al. (2001), we use the densities and the temperatures from our surface brightness and spectral fits to calculate the gas pressures in the free-stream region and in the galaxy gas just inside the edge, which is in pressure equilibrium with gas at the stagnation point (where the relative cluster gas velocity vanishes). The difference between the two pressures is interpreted as the ram pressure of the intracluster medium on the leading edge of the galaxy (the cold front), while the ratio of the pressures allows us to determine the Mach number $M_1 = v/c_1$ (where c_1 is the speed of sound in the cluster free-stream region) for the cold gas cloud moving through the hot ICM. The pressure jump versus Mach number relation, plotted in Figure 7, is given by

$$\frac{p_0}{p_1} = \left[1 + \frac{(\gamma - 1)}{2} M_1^2\right]^{(\gamma/\gamma - 1)} \quad (4)$$

for $M_1 \leq 1$ (subsonic regime), while

$$\frac{p_0}{p_1} = \left(\frac{\gamma + 1}{2}\right)^{(\gamma+1)/(\gamma-1)} M_1^2 \left(\gamma - \frac{\gamma - 1}{2M_1^2}\right)^{-1/(\gamma-1)} \quad (5)$$

for $M_1 > 1$ (supersonic regime), with $\gamma = 5/3$ the adiabatic index for a monatomic, ideal gas (Landau & Lifshitz 1959).

In Table 3 we summarize the results of this analysis for the best-fit temperatures and densities given in Tables 1 and 2. From Figure 7 we find a Mach number for the galaxy gas cloud

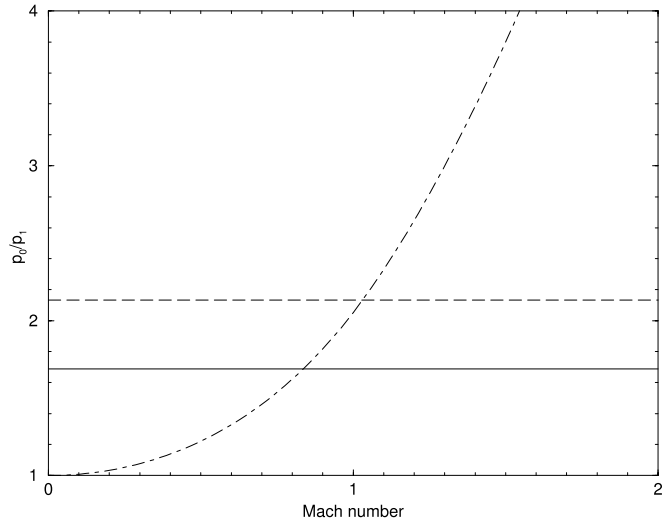

FIG. 7.—Pressure jump as a function of Mach number as given by eq. (4) for $M_1 < 1$ and eq. (5) for $M_1 > 1$ (*dot-dashed line*). The horizontal lines denote the value of the pressure jump for the PL+ICM1 model (*solid line*) and for the PL+ICM2 model (*dashed line*) fits to the surface brightness profile across the edge.

moving through the cluster gas of 0.83 (1.03) for the PL+ICM1 (PL+ICM2) best-fit density models. The sound speed for the completely ionized (mean molecular weight $\mu = 0.6$) intracluster gas at a temperature $1.53^{+0.10}_{-0.13}$ keV in the free-stream region is $c_1 = 638$ km s^{-1}. Thus, the speed $v = M_1 c_1$ of NGC 1404 relative to the ICM is found to be $v = 531$ (657) kms for these two models, in excellent agreement with the estimate ($v \sim 660 \pm 260$ km s^{-1}) by Scharf et al. (2004). If we assume that the Fornax Cluster ICM, or at least that part of it that impacts the leading edge of NGC 1404, is at rest relative to NGC 1399 and use the radial (line of sight) velocities 1947 km s^{-1} for NGC 1404 and 1425 km s^{-1} for NGC 1399 given in NED (Graham et al. 1998), then the radial velocity between these galaxies would be 522 km s^{-1}. The relative transverse component of the velocity between NGC 1404 and the Fornax ICM is then 98 and 399 km s^{-1} for our two models, respectively, implying an inclination angle for the motion with respect to the plane of the sky of $\xi \sim 79^\circ$ and 53°, respectively. However, Mazzotta et al. (2001) stress that the sharpness of the edge is a strong function of the inclination angle ξ. Given the sharpness of the observed edge in NGC 1404, these derived inclination angles are uncomfortably large. If we adopt instead the optical relative radial velocity $v_r = 450$ km s^{-1} measured by Drinkwater et al. (2001), who identify NGC 1404 as part of a larger, high-velocity, infalling Fornax subcluster, the inferred transverse velocities for NGC 1404 increase to $\sim$292 and 479 km s^{-1} for our two models, respectively. While improved, the inferred inclination angle of the motion with respect to the plane of the sky, $\xi = 58^\circ$ and 43°, respectively, is still large.

There are several possible solutions to this dilemma. First, NGC 1404 and 1399 may not both lie in the plane of the sky. NGC 1404 may be undergoing a flyby of the dominant elliptical galaxy, with a nonnegligible impact parameter rather than a direct collision, such that the use of the projected distance between the galaxies underestimates the physical radial distance between them and overestimates the value of the cluster electron density at the edge. Thus, the density jump should be viewed as a lower bound on the physical density discontinuity, Mach number, and relative velocity of NGC 1404 with respect to the intracluster gas. A second possibility is that NGC 1399 is moving with respect to the Fornax ICM and may itself be experiencing ram pressure stripping due to this motion (Paolillo et al. 2002). Then the optically measured relative radial velocity between the two galaxies may not accurately reflect the relative radial velocity between NGC 1404 and the surrounding cluster gas.

TABLE 3
DERIVED VELOCITIES AND EDGE PROPERTIES FOR TWO CLUSTER ICM MODELS

Property	PL+ICM1 Model	PL+ICM2 Model
n_{e0}/n_{e1}	4.78	6.04
T_0/T_1	0.36	0.36
p_0/p_1	1.7	2.1
M_1	0.83	1.03
v (km s^{-1})	531	657
v_t (km s^{-1})	98 (298)	399 (478)
ξ (deg)	79 (58)	53 (43)

NOTES.—n_e, T, and p denote the electron density, temperature, and pressure in each region specified by subscripts 0 and 1 for galaxy gas just inside the edge and cluster gas in the free-stream region, respectively (see Vikhlinin et al. 2001). M_1 is the Mach number, v is the relative total velocity, and v_t and ξ are the component of velocity in the plane of the sky and the inclination angle of motion with respect to the plane of the sky, respectively, assuming a relative radial velocity between NGC 1404 and 1399 of $v_r = 522$ km s^{-1} from NED ($v_r = 450$ km s^{-1} from Drinkwater et al. 2001).

We also note that the uncertainty in the electron density inside the edge in NGC 1404 due to uncertainties in the measured abundance in the galaxy gas causes similar uncertainties in the pressure ratio, i.e., $p_0/p_1 = 1.7^{+0.2}_{-0.4}$ for model PL+ICM1 ($2.2^{+0.2}_{-0.6}$ for model PL+ICM2), where the upper limit on the pressure ratio corresponds to the lower 90% confidence limit ($A = 0.56\ Z_\odot$) on the abundance in the two-component model for NGC 1404 and the lower limit on the pressure ratio corresponds to the supersolar ($A = 1.38\ Z_\odot$) upper limit on the abundance. This results in uncertainties in the velocity inferred for NGC 1404 of $v = 549^{+38}_{-192}$ km s^{-1} for model PL+ICM1 (676^{+32}_{-166} km s^{-1} for model PL+ICM2). The inferred velocity is less sensitive to a decrease in the galaxy abundance, as can be seen from Figure 7, because the pressure ratio versus Mach number curve steepens as the pressure ratio is increased. However, for the supersolar abundance in NGC 1404 implied by our 90% confidence upper limit, the pressure ratio corresponds to a subsonic velocity in Figure 7, where the curve flattens, such that the uncertainties in the velocity become large.

Despite these uncertainties, it is useful to consider what our analysis implies for the increased temperature and density expected in the stagnation region for the best-fit parameters. For the subsonic motion ($M = 0.83$) found for model PL+ICM1 and using the cluster-free stream as the reference region, Bernoulli's equation predicts a density increase of 37%, leading to a surface brightness enhancement by a factor of $\sim$1.9. This is consistent with the possible $\sim$70% surface brightness enhancement seen just outside the edge in Figure 5. The temperature in the stagnation region would be expected to rise by $\sim$23% by adiabatic compression to $\sim$1.88 keV. However, the stagnation region is small (of the order of a galaxy diameter) such that the observed temperature would be lower because of dilution by cooler cluster gas along the line of sight. Our measurements for the temperature in this region hint of a possible temperature rise consistent with such adiabatic heating, but, because of limited statistics, our errors are too large for a definitive measurement. For model PL+ICM2 ($M \sim 1.03$) the temperature and density

behind the shock would be expected to increase by ~3% and ~5%, respectively, with temperature and density in the stagnation region similar to that for model PL+ICM1. Such a weak shock would not be seen in our data.

4. CONCLUSIONS

In this paper we have used data from three *Chandra* observations using the ACIS array (a 57.4 ks exposure with chips S2 and S3 taken on 2000 January 18–19, a 29.6 ks exposure using chip S3 taken on 2003 February 13, and a 47.3 ks exposure using the ACIS-I array taken on 2003 May 28–29) of the elliptical galaxy NGC 1404 falling toward the dominant elliptical galaxy NGC 1399 in the Fornax Cluster to bound the relative physical motion of NGC 1404 with respect to the Fornax Cluster ICM. We find:

1. The temperature and abundance of the galaxy gas just inside the edge in NGC 1404 is $0.55^{+0.01}_{-0.02}$ keV and $0.73^{+0.65}_{-0.16}$ $Z_\odot$, typical of elliptical galaxies. Gas temperatures for the cluster gas in the free-stream region (W1) and the region next to the edge containing the stagnation point (W0) are $1.53^{+0.10}_{-0.13}$ and $1.66^{+0.25}_{-0.15}$ keV, respectively, with a cluster abundance of $0.42^{+0.2}_{-0.13}$ $Z_\odot$ measured in W1.

2. The X-ray emissivity in NGC 1404 is more than a factor of 2 greater than that of the surrounding cluster gas. Since the X-ray emissivity is dominated by line emission in cool, metal-rich galaxies, high-quality abundance measurements in galaxies are crucial for determining the density discontinuity across the edge and constraints on the dynamical motion of the galaxy through the ICM from these edge analyses.

3. The surface brightness profile in NGC 1404 in the direction toward NGC 1399 obeys a power law for 1 kpc $< r <$ 4 kpc, a break at ~4 kpc, and a sharp edge where the surface brightness decreases by more than an order of magnitude over 1–2 kpc. Outside the edge the surface brightness profile is consistent with cluster gas, with a possible 50%–70% enhancement at $r \sim 10$ kpc.

4. The best-fit edge position is found to be at 7.6–8.0 kpc from the center of the edge-bounding ellipse, with a weak dependence on the behavior of the cluster gas density at large radii from NGC 1399. A single PL density model within NGC 1404 provides a poor fit to the data for $r \gtrsim 4$ kpc. The surface brightness profile across the edge is well modeled with a PL electron density in NGC 1404 with index $\alpha = 1.54$ (β-model index $\beta = 0.47$) for 1 kpc $< r <$ 4 kpc, a break at ~4 kpc, after which α flattens to ~0.5–0.8, with a weak dependence on the β-model parameters assumed for the cluster gas. The sharpness of the edge is consistent with a jumplike density discontinuity with electron density in NGC 1404 inside the edge of $3.9–4.3 \times 10^{-3}$ cm^{-3}, and in the cluster free-stream region of $7–8 \times 10^{-4}$ cm^{-3}.

5. The pressure jump, $p_0/p_1 \sim 1.7–2.1$, between the cluster free-stream region and gas at the edge implies a Mach number $M_1 \sim 0.83–1.03$ relative to gas in the cluster free-stream region and thus a velocity $v \sim 531–657$ km s^{-1} for NGC 1404 through the surrounding ICM. This motion predicts an enhancement in the surface brightness of the cluster gas in the stagnation region by a factor of ~1.9 due to adiabatic compression, consistent with that seen.

6. Using values for the relative radial velocity between NGC 1404 and 1399 drawn from the literature as representative of the relative radial velocity between NGC 1404 and the surrounding cluster gas, the inferred value for the inclination angle of the motion with respect to the plane of the sky is large, $\gtrsim 40^\circ$, in apparent contradiction to the observed sharpness of the edge. This may signal the presence of a significant impact parameter between NGC 1404 and 1399, or that NGC 1399 is also moving radially with respect to the cluster gas. Thus, more detailed hydrodynamic modeling of this system is required to resolve the full three-dimensional motion of this system.

This work is supported in part by NASA contract NAS8-03060 and the Smithsonian Institution. M. E. M. acknowledges partial support from the Radcliffe Institute for Advanced Study at Harvard University. This work has made use of the NASA/IPAC Extragalactic Database (NED), which is operated by the Jet Propulsion Laboratory, California Institute of Technology, under contract with the National Aeronautics and Space Administration. We wish to thank Paul Nulsen for helpful discussions.

REFERENCES

AbdelSalam, H., Saha, P., & Williams, L. 1998, AJ, 116, 1541
Acreman, D., Stevens, I., Ponman, T., & Sakelliou, I. 2003, MNRAS, 341, 1333
Angelini, L., Loewenstein, M., & Mushotzky, R. 2001, ApJ, 557, L35
Bautz, M. W., et al. 1998, Proc. SPIE, 3444, 210
Brighenti, F., & Mathews, W. G. 1999, ApJ, 515, 542
Buote, D. 2002, ApJ, 574, L135
Buote, D., & Fabian, A. 1998, MNRAS, 296, 977
Dickey, J. M., & Lockman, F. J. 1990, ARA&A, 28, 215
Dosaj, A., Forman, C., Forman, W. R., Markevitch, M., & Vikhlinin, A. 2002, BAAS, 34, 712
Drinkwater, M., Gregg, M., & Colless, M. 2001, ApJ, 548, L139
Forman, W., Markevitch, M., Jones, C., Vikhlinin, A., & Churazov, E. 2001, in XXXVIth Rencontres de Moriond, XXIst Moriond Astrophysics Meeting, Clusters of Galaxies and the High Redshift Universe Observed in X-Rays: Recent Results from XMM-Newton and Chandra, ed. D. M. Neumann & J. T. T. Van (Paris: EDP), 33
———. 2002 in Lighthouses of the Universe: The Most Luminous Celestial Objects and Their Use for Cosmology (Berlin: Springer), 51
Forman, W., Schwarz, J., Jones, C., Liller, W., & Fabian, A. 1979, ApJ, 234, L27
Garmire, G. P., et al. 1992, in Proc. AIAA Space Prog. Tech. Conf. (New York: AIAA), 1473
Gnedin, O. Y. 2003, ApJ, 582, 141
Graham, A. W., Colless, M. M., Busarello, G., Zaggia, S., & Longo, G. 1998, A&AS, 133, 325
Heinz, S., Churazov, E., Forman, W., Jones, C., & Briel, U. G. 2003, MNRAS, 346, 13
Irwin, J. A., & Sarazin, C. 1996, ApJ, 471, 683
Jones, C., Stern, C., Forman, W., Breen, J., David, L., Tucker, W., & Franx, M. 1997, ApJ, 482, 143
Landau, L. D., & Lifshitz, E. M. 1959, Fluid Mechanics (London: Pergamon), chap. 9
Loewenstein, M., Mushotzky, R., Tamura, T., Ikebe, Y., Makishima, K., Matsushita, K., Awaki, H., & Serlemitsos, P. 1994, ApJ, 436, L75
Machacek, M. E., Bautz, M. W., Canizares, C. R., & Garmire, G. P. 2002, ApJ, 567, 188
Markevitch, M., et al. 2000, ApJ, 541, 542
Mazzotta, P., Markevitch, M., Vikhlinin, A., Forman, W. R., David, L. P., & VanSpeybroeck, L. 2001, ApJ, 555, 205
Morrison, R., & McCammon, D. 1983, ApJ, 270, 119
O'Sullivan, E., Ponman, T., & Collins, R. 2003, MNRAS, 340, 1375
Paolillo, M., Fabbiano, G., Peres, G., & Kim, D.-W. 2002, ApJ, 565, 883
Plucinsky, P. P., et al. 2003, Proc. SPIE, 4851, 89
Prigozhin, G. Y., Kissel, S. E., Bautz, M. W., Grant, C., LaMarr, B., Foster, R. F., Ricker, G. R., Garmire, G. P. 2000, Proc. SPIE, 4012, 720
Rangarajan, F. V. N., Fabian, A. C., Forman, W. R., & Jones, C. 1995, MNRAS, 272, 665

Scharf, C. A., Zurek, D. R., & Bureau, M. 2004, preprint (astro-ph/0406216)
Schindler, S., Binggeli, B., & Böhringer, H. 1999, A&A, 343, 420
Smith, R. K., Brickhouse, N. S., Liedahl, D. A., & Raymond, J. D. 2001, ApJ, 556, L91
Vikhlinin, A., Markevitch, M., & Murray, S. S. 2001, ApJ, 551, 160
Wang, Q. D., Owen, F., Ledlow, M., & Keel, W. 2004, in Proc. IAU Colloq. 195, Outskirts of Galaxy Clusters: Intense Life in the Suburbs, ed. A. Diaferio (Cambridge: Cambridge Univ. Press), 78
White, D., Fabian, A., Forman, W., Jones, C., & Stern, C. 1991, ApJ, 375, 35